RESEARCH PAPER

# Numerical analysis of electrokinetic transport in micro-nanofluidic interconnect preconcentrator in hydrodynamic flow

**Yi Wang · Kapil Pant · Zhijian Chen · Guiren Wang · William F. Diffey · Paul Ashley · Shivshankar Sundaram**

**Abstract** The phenomenon of enrichment of charged analytes due to the presence of an electric field barrier at the micro-nanofluidic interconnect can be harnessed to enhance sensitivity and limit-of-detection in sensor instruments. We present a numerical analysis framework to investigate two critical electrokinetic phenomena underlying the experimental observation in Plecis et al. (Micro Total Analysis Systems, pp 1038–1041, 2005b): (1) ion transport of background electrolytes (BGE) and (2) enrichment of analytes in the micro-nanofluidic devices that operate under hydrodynamic flow. The analysis is based on the full, coupled solution of the Poisson–Nernst–Planck (PNP) and Naviér–Stokes equations, and the results are validated against analytical models of simple canonical geometry. Parametric simulation is performed to capture the critical effects of pressure head and BGE ion concentration on the electrokinetics and ion transport. Key findings obtained from the numerical analysis indicate that the hydrodynamic flow and overlapped electrical double layer induce concentration–polarization at the interfaces; significant electric field barrier arising from the Donnan potential forms at the micro–nano interfaces; and streaming potential and overall potential are effectively established across the micro-nanofluidic device. The simulation to examine analyte enrichment and its dependence on the hydrodynamic flow and analyte properties, demonstrates that order-of-magnitude enrichment can be achieved using properly configured hydrodynamic flow. The results can be used to guide practical design and operational protocol development of novel micro-nanofluidic interconnect-based analyte preconcentrators.

## List of symbols

| | |
|---|---|
| $c$ | Concentration of species and analytes |
| $D$ | Molecular diffusivity of species |
| $e$ | Elementary charge |
| $E$ | Electric field strength |
| $f_e$ | Electrostatic body force |
| $F$ | Faraday constant |
| $\hat{i}$ | Unit vector normal to the channel's cross-section |
| $I$ | Electric current |
| $J$ | Species flux |
| $k$ | Boltzmann constant |
| $L_x$ | Channel length |
| $R$ | Gas constant |
| $S$ | Channel's cross-section |
| $t$ | Time, s |
| $T$ | Absolute temperature |
| $\mathbf{u}$ | Velocity vector |
| $w$ | Width of nanochannels/microchannels |
| $x$ | Streamwise coordinate |
| $y$ | widthwise coordinate |
| $z$ | Valence |

## Greek symbols

| | |
|---|---|
| $\varepsilon_0$ | Electrical permittivity of the vacuum |
| $\varepsilon_r$ | Relative permittivity |
| $\phi$ | Electrical potential |
| $\phi_s$ | Surface potential |
| $\kappa$ | Inverse of Debye length |
| $\mu$ | Dynamic viscosity of fluid |

Y. Wang (✉) · K. Pant · Z. Chen · S. Sundaram
CFD Research Corporation, Huntsville, AL 35805, USA
e-mail: yxw@cfdrc.com

G. Wang
Department of Mechanical Engineering,
University of South Carolina, Columbia, SC 29208, USA

W. F. Diffey · P. Ashley
U.S.Army RDECOM, Redstone Arsenal, AL 35898, USA

| $v$ | Ion mobility |
| --- | --- |
| $\rho$ | Fluid density |
| $\rho_e$ | Volumetric charge density |
| $\sigma$ | Surface charge density |
| $\omega$ | Electrophoretic mobility |
| $\Gamma$ | Electrical current density |
| $\Psi$ | Distribution of normalized electrical potential |
| $\Psi_s$ | Normalized surface potential |
| $\zeta$ | Zeta potential |

**Subscripts/Superscripts**

| $A,B,C$ | Analytes A, B, C |
| --- | --- |
| anal | Analyte |
| bulk | Bulk solution |
| conv | Convection |
| $D$ | Diffusion |
| elec | Electromigration |
| $i$ | The $i$th species |
| tot | Sum of all species |
| $+$ | Positive mono-valence |
| $-$ | Negative mono-valence |
| $\perp$ | Normal component |

## 1 Introduction

Analyte preconcentration, which concentrates (or focuses) small amounts of analyte molecules into reduced volume, is recognized as one of the most critical steps in integrated lab-on-chip systems for genomic, proteomic, and clinical applications. The significance of analyte preconcentration lies in the alleviation of the sensitivity requirements of the sensing modalities, thereby improving their integrability with microfluidic platforms (Lichtenberg et al. 2002; Shackman and Ross 2007; Sueyoshi et al. 2008). Currently, a variety of preconcentration methods have been successfully developed in conjunction with the microfluidic analysis and proven to be effective in terms of enhancing analysis performance, such as conductivity gradient focusing, electric-field gradient focusing, field-amplified sample stacking, and temperature-gradient focusing (Shackman and Ross 2007; Sueyoshi et al. 2008). Recently, preconcentration that exploits the electrokinetic trapping mechanism at the micro–nano channel interface has been reported (Wang et al. 2005; Kim et al. 2006). In addition to ultra-high enrichment ratios, the analyte preconcentration based on micro–nano channel interfacial electrokinetics bears several notable features, such as operating simplicity and integrability, and hence, hold great promise for micro-total-analysis systems. Its underlying principle relies on the overlapped electric double layer (EDL) and non-electro-neutral background electrolyte (BGE) concentrations in the nanochannel, which gives rise to an extended depletion layer repelling analytes (carrying similar charges as the nanochannel wall) from entering the nanochannel.

The origin of related electrokinetics can be traced back to the early study of ion-selective porous media (refer to (Leinweber et al. 2005; Jin et al. 2007; Ehlert et al. 2008; Huang and Yang 2008) for a comprehensive historical view of the progression of the theory). The recent advent of the MEMS and micro- and nano-fluidic technology has aroused significant research interests and efforts devoted to understanding and applying this phenomenon for sample preconcentration in integrated lab-on-a-chip applications. Both experimental and modeling studies have been extensively conducted for these investigations. Studies by Pu et al. (2004) observed ion enrichment and depletion phenomena at the micro–nano interfaces, and found that the intensity of the enrichment and depletion depends on the extent of double-layer overlap. Ion enrichment and depletion effects and its consequences on the permselectivity of the nanochannel were quantitatively studied by Plecis et al. (2005a). In their study, the effect of surface pretreatment on the stability of the BGE-channel wall interaction was experimentally investigated and a simple model assuming Poisson–Boltzmann equation was formulated to capture the diffusive transport of the charged ion species. Recently, ionic depletion and enrichment, particularly in the nonlinear electrokinetic regime and induced electroosmotic flow (of the second kind) and vortex flow structures were also investigated (Kim et al. 2007; Huang and Yang 2008). The dependence of the current and sizes of the depletion regions on the applied voltage/field was explicitly determined. In addition to the experiments, high-fidelity computational analysis has also been utilized to enable a thorough spatio-temporal understanding of the phenomena. Daiguiji et al. presented a series of analysis regarding the ionic distribution transport with applied electric field or under pressure driven flow (Daiguji et al. 2004a, b, 2005, 2006), in which continuum dynamics and Poisson–Nernst–Planck (PNP) equations are solved for calculations. The ion enrichment and depletion, and unipolar solution of counterions for large Deybe length were numerically demonstrated. The applicability of the nanofluidic electrokinetics for a unipolar ionic field-effect transistor and electrochemomechanical energy conversion were also discussed in detail. Jin et al. conducted temporal analysis of the electrokinetic transport in a micro-nanofluidic interconnect under three operating stages (Jin et al. 2007), i.e., rest, injection, and recovery. Among other key findings, they captured the nonlinear electrokinetic behavior at the recovery stage due to the induced pressure, electroosmotic flow of the second kind, and complex flow circulation. Finite element method was also used in Mansouri et al. (2005) to study transient streaming potential in a finite length microchannel of circular cross-section with the

emphasis on the different time scales of establishing the streaming potential and the ion concentration field. The advancement in theory inspires the use of such nano-electrokinetic phenomena for sample preconcentration in a diversity of LoC bioanalysis systems. Wang et al. developed a highly efficient continuous sample preconcentration device for proteins and peptides (Wang et al. 2005), with enrichment factors as high as $10^6$–$10^8$. A protein concentration device integrated with an electrophoretic separation component was reported by Kim et al. (2006). Different from the lateral flow mode used by Wang et al. (2005), their device relies on the frontal electrokinetic flow through the micro-nanochannel interface. Enrichment ratios up to $10^6$ in 30 min were demonstrated and protein peaks of BSA and VOA were clearly resolved in 2 min. Recently, Wang et al. also demonstrates the strength of the nano-preconcentrator in terms of enhancing immunoassay detection sensitivity and binding kinetics (Wang and Han 2008). They presented a device consisting of a preconcentrator and a bead-based immunoassay. With a 30 min preconcentration, the immunoassay sensitivity was increased by more than 500 fold (from 50 pM to the sub 100 fM range). Moreover, the detection range of the given bead-based assay can be flexibly modulated from 10–10,000 to 0.01–10,000 ng ml$^{-1}$ by varying the preconcentration time.

In addition to applied electric field, pressure driven flow also enables sample preconcentration at the micro–nano interface. It was demonstrated by Plecis et al. (2005b) that the ion exclusion effects enable analyte enrichment when the analyte solution is forced through the nanochannel by a pressure gradient, although the mechanism underlying the observation is not yet clear.

Built on the broad spectrum of relevant works in this area, this paper presents a multi-physics framework for numerical analysis to investigate electrokinetics and analyte preconcentration in the micro-nanofluidic interconnect under hydrodynamic flow. Our study captures critical phenomena of ion transport at the micro–nano interface (such as ion enrichment and depletion, i.e., concentration polarization, and induced potential and electrical field) and evaluates the effects of the operating parameters and analyte properties on the preconcentration performance. The analysis is based on continuum dynamics and coupled calculation of the governing equations. The simulation results are validated using analytical forms and numerical data reported in the literature (Daiguji et al. 2004a; Feng et al. 2006). The numerical analysis and findings in this paper can be utilized to guide design and protocol development of analyte preparation for microfluidic analysis.

Compared to previous studies, our effort exhibits two significant novelties. First, our study focuses on the nano-scale electrokinetics and induced electrical characteristics in hydrodynamic flow underlying the experimental observation by Plecis et al. (2005b) rather than the applied electrical field. Our effort investigates the impacts of pressure head and BGE concentrations that serve as the primary, post-fabrication means of modulation of ion transport and analyte enrichment. Second, in contrast to the previous numerical studies on electrochemomechanical conversion (Daiguji et al. 2004b, 2006), our emphasis is to capture ion transport equilibrium and induced electrical field at the micro–nano interface, in particular for analyte preconcentration.

The paper is organized as follows. The micro-nanofluidic preconcentrator, computational models (i.e., governing equations), and numerical methods (such as assumptions and boundary conditions) are first briefly introduced in Sect. 2. In Sect. 3, the numerical models are validated using analytical solution and relevant numerical data, which is then followed by the parametric analysis of the effects of the pressure head and BGE concentration. Simulation of the analyte preconcentration process is given in Sect. 3.3. The paper concludes with a summary in Sect. 4.

## 2 Models and numerical methods

In this section, the micro-nanofluidic preconcentrator in hydrodynamic flow is introduced. The simulation methods, as well as the assumptions used in the numerical analysis are presented.

### 2.1 Micro-nanofluidic preconcentrator

Figure 1a illustrates the geometry and schematic of the hydrodynamic flow based micro-nanofluidic interconnect preconcentrator in our analysis. A negatively charged nanochannel bridges two microchannels (or micro-reservoirs). The nanochannel is 1 μm long and 50 nm high and the microchannel has a length of 2 μm and a height of 1.05 μm. The third dimension (the other transverse dimension) perpendicular to the paper has a unit width. A pressure head ($\Delta p$ relative to the outlet) is applied at the inlet, driving the BGE solution from right to the left and carrying BGE ions and sample analytes towards the micro-nanochannel interface. Different from the microchannel containing electroneutral bulk BGE, the nanofluidic channel is characterized by an overlapped EDL of BGE ions. A substantial electric field barrier/exclusion at the right interface originating from the Donnan potential (Probstein 2003) is induced and is directed to the left. The field imposes electrophoretic force (pointing to the right) on the negatively charged analytes to oppose the hydrodynamic force and precludes the analyte from entering the nanochannel. Thus, a region of zero overall velocity is present around the interface, where the analyte is trapped and

**Fig. 1** Schematics of the micro-nanofluidic interconnect preconcentrator. **a** Geometry and operating parameters in numerical analysis. **b** Mechanism of the hydrodynamic flow-driven preconcentration. **c** Mechanism of electric field-driven preconcentration
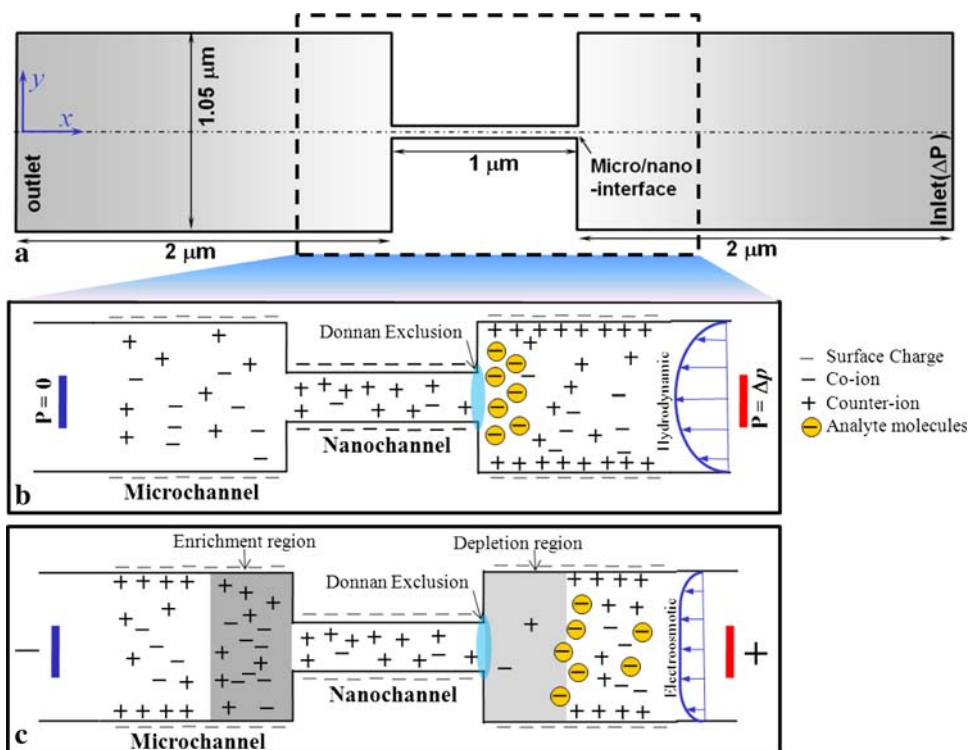


enriched (Shackman and Ross 2007) (see Fig. 1b). As the flow continuously carries analytes toward the interface, the analyte keeps accumulating until the local equilibrium of convective–diffusive-electromigratory analyte transport is reached. To achieve adequate analyte enrichment in reasonable processing time, strong electric field barrier/exclusion and fast hydrodynamic flow are both desired. It is interesting to note that this is inherently different from electric field-activated preconcentration (Fig. 1c). Under applied electric field, on the anodic side, positive BGE ions can enter the nanochannel, while negative ions are driven away from the nanochannel, leading to ion depletion at the anodic side of the nanochannel (Wang et al. 2005; Kim et al. 2007; Huang and Yang 2008; Wang and Han 2008). At high electric field, an extended space charge layer will be formed herein, which exerts considerable repulsive force (pointing to the right) on the negatively charged analyte molecules (Wang et al. 2005). The dominant electroosmotic flow continuously transports negatively charged analyte molecules towards the region to achieve preconcentration.

## 2.2 Models and governing equations

Prior studies (Daiguji et al. 2004a; Jin et al. 2007) have shown that for dimension scale larger than 5–10 nm, continuum dynamics is a precise description of BGE transport, which is also used for our model formulation given the fact that the smallest dimension in hydrodynamic flow

preconcentrator is 50 nm. Three sets of equations, i.e., Poisson equation, Nernst–Planck equation, and Naviér–Stokes equation are employed to resolve the electric potential/field, species distribution, and fluid flow, respectively (Daiguji et al. 2004a, b, 2006; Jin et al. 2007).

The Poisson equation, the differential form of the Gaussian law, is expressed as

$$\nabla \cdot (\varepsilon_r \nabla \phi) = -\frac{\rho_e}{\varepsilon_0} \tag{1}$$

where $\phi$ is the electrical potential, from which electric field can be obtained by $E = -\nabla \phi$; $\varepsilon_0$ and $\varepsilon_r$ are the electrical permittivity of the vacuum and the relative permittivity, respectively; $\rho_e$ is the volumetric charge densities of the ionic species. For a system involving $n$ ionic species, $\rho_e$ is given by

$$\rho_e = F \sum_{i=1}^{n} z_i c_i \tag{2}$$

The species transport is governed by the Nernst–Planck (NP) equation (Masliyah and Bhattacharjee 2006),

$$\frac{\partial c_i}{\partial t} + \nabla \cdot J_i = 0 \tag{3}$$

and

$$J_i = -D_i \nabla c_i + \mathbf{u} c_i - \omega_i z_i c_i \nabla \phi \tag{4}$$

where $c_i$ is the concentration of the $i$th species, and $J_i$ is the flux of the $i$th species; $\mathbf{u}$ is the velocity vector; $\omega_i$ and $D_i$

are the electrophoretic mobility and diffusivity of the species; $z_i$ is the valence of the species. The terms on the R.H·S. of Eq. 4 denote the flux contributions from molecular diffusion, convection, and electromigration, respectively. Note that Eq. 4 applies to both BGE ions and analytes. For BGE ions, $\omega_i = Fv_i$, where $F$ is the Faraday constant, $v_i$ is the mobility of the ion and can be obtained from the Nernst–Einstein equation $v_i = D_i/RT$ (Masliyah and Bhattacharjee 2006). The electrical current in the solution is a result of the overall charge movement due to individual flux of BGE ions and is written as

$$\Gamma_i = Fz_iJ_i = F\left(-z_iD_i\nabla c_i + \mathbf{u}z_ic_i + \omega_iz_i^2c_i(-\nabla\phi)\right)$$

$$\Gamma_{\text{tot}} = \sum_{i=1}^n \Gamma_i = F\sum_{i=1}^n z_iJ_i$$

$$I_{\text{tot}} = \int_S \Gamma_{\text{tot}}\cdot \mathrm{d}S = I_{\text{tot},D} + I_{\text{tot,conv}} + I_{\text{tot,Elec}} = 0$$

$$(5)$$

where $\Gamma_i$ is the current density contributed by the $i$th ion, and the three terms on the R.H·S of the first equation signify the contributions from diffusion, convection, and electromigration, respectively. $\Gamma_{\text{tot}}$ is the current density summed over all ions. $I_{\text{tot}}$ is the total electrical current flow, and likewise it contains three components arising from diffusion ($I_{\text{tot, }D}$), convection ($I_{\text{tot, conv}}$), and electromigration ($I_{\text{tot, Elec}}$). $\mathrm{d}S$ is the differential surface element on the channel's cross-section ($S$). It should be noted that while there is no overall current (i.e., $I_{\text{tot}} = 0$ along the channel) in the hydrodynamic preconcentrator, the current components $\Gamma_i$ can be non-zero. For a system containing a symmetric monovalence BGE pair, the flux of the total electric current in Eq. (5) can be simplified as

$$I_{\text{tot}} = \int_S \Gamma_{\text{tot}}\cdot \mathrm{d}S, \Gamma_{\text{tot}} = F(-D\nabla(c_+ - c_-) + \mathbf{u}(c_+ - c_-)$$
$$+ \omega(c_+ + c_-)(-\nabla\phi))$$
$$(6)$$

where for brevity, a single diffusivity $D$ and mobility $\omega$ are used for both positive and negative ions in Eq. 6. It indicates that $\Gamma_{\text{tot}}$ heavily depends on the concentration difference between positive and negative ions ($c_+ - c_-$), the gradient of their difference $\nabla(c_+ - c_-)$, total ion concentrations ($c_+ + c_-$), flow velocity and electric field as well.

Viscous, incompressible fluid flow in the micro- and nano-channels is described by the conservation of mass and Naviér–Stokes (momentum) equations,

$$\nabla \cdot \mathbf{u} = 0$$
$$\frac{\partial \mathbf{u}}{\partial t} + (\mathbf{u}\cdot\nabla)\mathbf{u} = \mu\nabla^2\mathbf{u} - \nabla p/\rho + f_e$$
$$(7)$$

where $\mathbf{u}$, $\rho$, $\mu$, and $p$ are the fluid velocity, density, dynamic viscosity, and pressure, respectively; $f_e$ is the electrostatic body force due to the electrostatic charges (Columbic force) and is expressed as $f_e = -\rho_e\nabla\phi$.

## 2.3 Numerical methods

Numerical analysis is performed using the multi-physics, finite volume-based simulation software, CFD-ACE + (ESI-CFD, Inc.). The computational domain is meshed by a block-structured grid using the preprocessor (CFD-GEOM) available within CFD-ACE+. Three key modules—fluid flow, electric, and chemistry—are invoked to solve the fluid flow velocity, electric potential and field, and species distribution, respectively. The CFD-ACE+ solver uses the SIMPLEC algorithm for pressure–velocity coupling (Patankar 1980). An upwind scheme is used for discretization of the velocity fields, while a second-order scheme is used for analyte distribution. The linearized algebraic equations are solved using an algebraic multi-grid (AMG) iterative method for accelerated convergence. The electrostatic body force $f_e$ term in the Naviér–Stokes equation (i.e., Eq. 7) is implemented using a user-defined subroutine.

As preconcentrators are typically designed to target analytes at trace-level concentrations (picomolar–nanomolar), we assume that the analyte concentration is so dilute that its presence does not alter the electric field and flow field established by the BGE ions. Following the regular perturbation analysis by Bharadwaj and Santiago (2005), our simulation is conducted in two steps. In the first step, Eqs. (1), (3), and (7) are solved in a coupled manner to resolve electric potential ($\phi$), BGE ion concentrations ($c$), and the flow field ($\mathbf{u}$). In the second step, Eq. 3 is solved for the analyte concentrations with $\mathbf{u}$ and $\phi$ obtained from the first step. This approach is most suitable for systems involving dilute analytes, which is typical for a variety of proteomic, genomic, and chemical compound analysis.

Boundary conditions are also supplied for closure of the equations. Electrically, following (Daiguji et al. 2004a, 2006), a fixed surface charge density is specified at the nanochannel walls with a typical value of $\sigma = -0.002$ C/m$^2$. Charges on the microchannels are neglected. Zero potential is assumed at the microchannel outlet, and zero surface charge density (i.e., zero electric field according to $\nabla_\perp\phi = -\sigma/\varepsilon_0\varepsilon_r$) is set at the inlet to ensure no overall current flow through the system (Daiguji et al. 2006; Masliyah and Bhattacharjee 2006), where $\perp$ denotes the normal component. For BGE flow, differential pressure ($\Delta p$) is applied at the inlet relative to the outlet. No-slip boundary conditions are invoked at all channel walls ($\mathbf{u} = 0$). For BGE ion transport, a constant bulk ion concentration ($c_{\text{bulk}}$) is provided at both the inlet and outlet (Daiguji et al. 2004a, 2006; Mansouri et al. 2005). For

**Table 1** Boundary conditions used in the numerical simulation

| | Inlet | Outlet | Microchannel wall | Nanochannel wall |
|---|---|---|---|---|
| Electrostatics | $\sigma = 0$ | $\phi = 0$ | $\sigma = 0$ | $\sigma = -0.002$ C/m$^2$ |
| BGE species | $c = c_{\text{bulk}}$ | $c = c_{\text{bulk}}$ | $J_\perp = 0$ | $J_\perp = 0$ |
| Analyte species | $c_{\text{anal,in}} = 1$ nM | $\nabla_\perp c = 0$ | $J_\perp = 0$ | $J_\perp = 0$ |
| Fluid flow | $P = \Delta p$ | $P = 0$ | $\mathbf{u} = 0$ | $\mathbf{u} = 0$ |

analyte transport, a constant sample concentration ($c_{\text{anal,in}}$) is set at the microchannel inlet. Table 1 summarizes all the boundary conditions used in the present simulation.

In this paper, potassium chloride (KCl) that can fully disassociate into K$^+$ and Cl$^-$ ions in the aqueous solution is used as the BGE. The diffusivity of K$^+$ and Cl$^-$ ions are $1.97 \times 10^{-9}$ m$^2$/s and $2.01 \times 10^{-9}$ m$^2$/s, respectively, and their mobility can be readily calculated using Nernst–Einstein equation. During experimentation, given a preconcentrator of fixed geometry, BGE concentration and pressure head (or flow rate) serve as primary means to modulate the operation and performance of the device. Therefore, these two parameters are interrogated in detail in our parametric analysis. Specifically, BGE concentration varies from 0.02 to 1 mM, all producing overlapped EDLs (but to different extents). The differential pressure varies from 0.1 to 0.4 atm. Table 2 lists the relevant parameters used in the parametric simulations along with the associated Péclet number $P_e = U/\kappa D$ and dimensionless pressure $\bar{P} = \Delta p z^2 e^2 / \varepsilon_0 \varepsilon_r k^2 T^2 \kappa^2$ (Masliyah and Bhattacharjee 2006), where $U$ is the average velocity in the nanochannel in the absence of surface charges, $\kappa$ is inverse of the Debye length, $e$ is the elementary charge, $k$ is the Boltzmann constant, $T$ is temperature. As molecular diffusivity of K$^+$ and Cl$^-$ are almost same, a single Péclet number is defined for both. In Table 2 Case 2 represents the baseline. The effects of pressure head and BGE ion concentrations are, respectively, captured by Cases 1, 2, and 3, and Cases 2, 4 and 5.

Grid checks are performed to ensure mesh-independent results. Specifically, $61 \times 51$ grid-points in a power law distribution are used to resolve the longitudinal and transverse dimensions of the nanochannel.

Several assumptions are invoked in the model formulation to render the simulation computationally efficient without appreciable compromise in accuracy. These include: (1) all simulations are performed in two-dimensional domain by assuming the other transverse dimension substantially exceeds the nano-scale; (2) water disassociation effect is neglected, i.e., H$^+$ and OH$^-$ ions are dilute, and electric current flow can exclusively be attributed to the movements of the BGE ions (Daiguji et al. 2004a, b, 2005, 2006; Jin et al. 2007); (3) after preconcentration, the analyte at the interface is still assumed dilute relative to the BGE; and (4) in the simulation we assume no electric charge at the microchannel wall, which has been used in previous numerical studies of micro-nanofluidic systems (Daiguji et al. 2004a, b, 2006). In hydrodynamic flow-driven case (see Fig. 1), the electro-viscous effect introduced by the surface charges on the microchannel is negligible due to the overwhelming dominance of the fluidic and electro-viscous resistance of the nanochannel in our simulation. In addition, as the microchannel around the interface is perpendicular to the nanochannel, the presence of electric charge on microchannel does not qualitatively alter the local electrokinetic behavior.

## 3 Result and analysis

In this section, the model is first validated by comparison with the analytical solutions using simple, canonical cases. Then parametric simulation of all cases in Table 2 is performed to capture the electrokinetics and ion transport in the micro-nanofluidic system under various operating conditions. Finally, transient simulation results of analyte transport and enrichment at the micro–nano interface are presented.

### 3.1 Model validation

In this section, our numerical models are validated in terms of BGE concentration, flow velocity, and current flow. Our model was previously compared with the finite difference methods (FDM)-based numerical simulation and data of ion transport in a 2D micro-nanochannel system involving strongly overlapped EDL (Daiguji et al. 2004a; Feng et al. 2006). In this paper, we further compare our simulation with analytical models using canonical, one-dimensional cases, which separately examine the validity of the numerical models in transverse and longitudinal directions of the

**Table 2** Simulation parameters for numerical analysis

| Case no. | 1 | 2 | 3 | 4 | 5 |
|---|---|---|---|---|---|
| BGE conc (mM) | 0.1 | 0.1 | 0.1 | 0.02 | 1 |
| $\Delta p$ (atm) | 0.1 | 0.2 | 0.4 | 0.2 | 0.2 |
| $P_e$ | 0.0307 | 0.0614 | 0.123 | 0.137 | 0.0194 |
| $\bar{P}$ | 20.2 | 40.3 | 80.7 | 202 | 4.03 |

channel (Daiguji et al. 2004a). A simple system includes two negatively charged ($\sigma = -10^{-3}$ C/m$^2$) channel walls that are 1 μm long and separated by a distance of 0.5 μm. KCl solution of $c_{bulk} = 0.1, 1,$ and 10 mM is contained in the system.

First, we verify the model in the *transverse* direction of the channel. As EDL thickness is small relative to the inter-wall spacing, we can assume Boltzmann distribution of electrolyte ions and integrate the Poisson equation in Eq. 1 to obtain the electric potential within the channel, which is

$$\Psi = 2 \ln \left[ \frac{1 + \exp(-\kappa y) \tanh(\Psi_s/4)}{1 - \exp(-\kappa y) \tanh(\Psi_s/4)} \right] \quad (8)$$

where $\Psi_s = ze\phi_s/kT$ and $\Psi = ze\phi/kT$ are, respectively, the normalized surface potential and the normalized potential distribution (Masliyah and Bhattacharjee 2006). Because of the electroneutrality, the electric charge in solution must balance the charge on the channel surface. Integrating Eq. 1 along the transverse direction of the channel yields

$$\sigma = - \int_0^{bulk} \rho_e \, dy = \varepsilon_0 \varepsilon_r \int_0^{bulk} \frac{d}{dy} \left( \frac{d\phi}{dy} \right) dy \quad (9)$$

Substituting Eq. 8 into Eq. 9, we can obtain the well-known Grahame equation (Daiguji et al. 2004a) that relates potential and charge at the channel surface,

$$\phi_s = \frac{2kT}{e} \sinh^{-1} \left[ \frac{\sigma}{(8\varepsilon\varepsilon_0 kT c_{bulk} N_a)^{1/2}} \right] \quad (10)$$

where $N_a$ is the Avogadro number. Likewise, the fluid velocity can be obtained by integrating the Naviér–Stokes equation, viz., Eq. 7 from the channel surface to the bulk solution, which reads (Xuan and Li 2004; Masliyah and Bhattacharjee 2006)

$$\mathbf{u} = -\frac{\varepsilon\varepsilon_0 \phi_s}{\mu} (\phi/\phi_s - 1)\nabla\phi \quad (11)$$

Numerical and analytical results (not shown) have excellent agreement in terms of electric potential and flow velocity with the worst relative error of 1.1%.

For validation in the *longitudinal* direction, we assume a uniform channel without surface charges, in which constant BGE concentrations $c_{bulk}$ are specified at both longitudinal ends. Thus, the electrical and ionic distributions along the transverse direction are negligible, and electric field along the longitudinal direction $x$ is a constant value of $-\nabla\phi = -\Delta\phi/L_x$, where $L_x$ is the channel length. From Eqs. 4 and 5, the current flux of individual species and the total flux are given by

$$\Gamma_i = -F \left( D_i \frac{Fz_i c_{bulk}}{RT} \nabla\phi \right), \Gamma_{tot} = \sum_i \Gamma_i \quad (12)$$

If the BGE (KCl) concentration $c_{bulk}$ is 0.1 mM and the potential difference across the channel is 0.01 V, the ionic current contribution of K$^+$ and Cl$^-$ and the total current calculated with Eq. 12 are, respectively, 7.36, 7.624, and 14.984 mA/m$^2$. The numerical simulation using PNP equation yields 7.31, 7.58, and 14.89 mA/m$^2$, respectively, showing a relative error less than 1%.

### 3.2 Parametric analysis of electrokinetic behavior

In this section, we present the parametric simulation results in steady state and analyze the influence of pressure head (or flow) and BGE ion concentrations on the ion transport and electrokinetics (in particular, the electrical field distribution) in the nanofluidic preconcentrator. Unless otherwise noted, longitudinal ($x$) profiles of all variables of interest are reported at the channel centerline, i.e., dash-dot line in Fig. 1; and the transverse ($y$) distributions are taken at the horizontal midpoint of the nanochannel.

#### 3.2.1 Effects of pressure head

Our analysis begins with the longitudinal profile of BGE ion concentrations at different pressure head (Cases 1–3) as shown in Fig. 2a. Several important features are observed: (1) within the nanochannel, the concentration of counter-ion (K$^+$) is significantly higher than the co-ion (Cl$^-$) to neutralize the negative charges on the channel wall; (2) in the microchannel, concentrations of both ions are almost the same as bulk concentration to satisfy electroneutrality, i.e., $\sum z_i c_i = 0$. As a result, steep gradients of the BGE ion concentrations form at the micro–nano interfaces of both sides; (3) relative to the bulk concentration in the micro-channel, BGE ions accumulate at the interface on the right (termed enrichment interface) and deplete at the left (termed depletion interface), viz., concentration–polarization (Daiguji et al. 2006). The ion accumulation at the enrichment interface is attributed to the imbalance in BGE ion flux therein. Hydrodynamic flow carries more co-ion (Cl$^-$) flux to the interface than that through the nano-channel due to the negative charges on the nanochannel walls that inhibit the passage of the co-ions, leading to the buildup of the co-ion around the junction region. The concentration of counter-ion (K$^+$) also arises in front of the junction to maintain electroneutrality (Jin et al. 2007). At the other side of the nanochannel, the co-ion flux through the nanochannel is insufficient to compensate for that taken away by hydrodynamic flow to the outlet. As a result, depletion of both co-ion and counter-ion forms to hold the electroneutrality. Given the same geometry, BGE concentration, and surface charges, the extent of ion accumulation/depletion is more marked at larger pressure
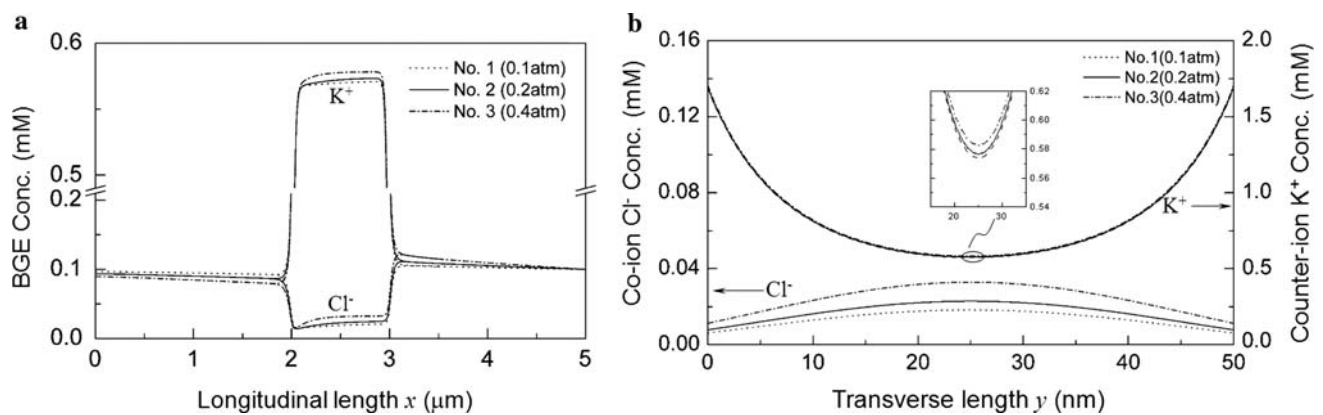
**Fig. 2** Profiles of BGE ion concentrations. (**a**) Longitudinal profile (**b**) Transverse profile

head (flow rate) due to the exacerbated imbalance in ion transport. It should be pointed out that the formation of ion accumulation/depletion in hydrodynamic flow is by nature different from that in the applied electric field. During the equilibration process, the hydrodynamic force is non-selective, driving both co- and counter-ions in the same direction, while under external electric field both ions experience electrophoretic forces in reverse directions.

Figure 2b illustrates the transverse concentration profiles of both BGE ions and indicates that a strongly overlapped EDL is established in the nanochannel. The channel is essentially filled with a unipolar solution of counter-ion $K^+$, that is, the solution is dominated by $K^+$ ions (note that different scales are used for $K^+$ and $Cl^-$ ions in Fig. 2b). Given same buffer conditions and nanochannel surface charges, larger pressure head generates faster flow speed and carries more BGE ions to the enrichment interface, leading to more appreciable ion buildup as discussed above. Therefore, slightly higher BGE concentration occurs at larger pressure head. Such a correlation between the transverse BGE ion profile and the pressure head (or flow rate) captured by our numerical analysis is absent in the classical 1D EDL model (Probstein 2003; Masliyah and Bhattacharjee 2006). It is interesting to point out that the difference between the curves of counter-ion and co-ion is proportional to the volumetric charge density (see Eq. 2); and hence, the area enclosed by both curves remains constant regardless of BGE concentrations and represents the total charges in solution to neutralize those on the nanochannel walls.

Figure 3 depicts the longitudinal dependence of the electrical potential (Fig. 3a) and field (Fig. 3b). It is interesting to note that while the potential difference between the inlet and the outlet is small (–0.1–0 V), the potential variation along the longitudinal direction is non-monotonic, which is in distinct contrast to ion accumulation/depletion using externally applied electrical field
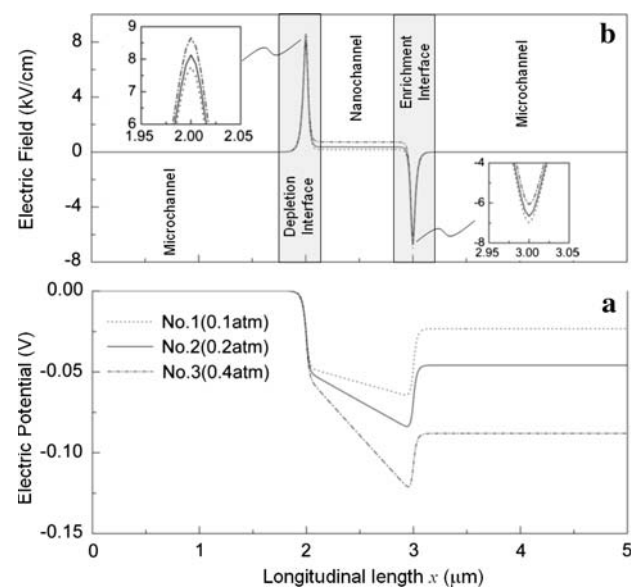


**Fig. 3** Longitudinal profiles of (**a**) electrical potential and (**b**) field

(Daiguji et al. 2004a). We can see that the longitudinal potential profile comprises of three parts: constant potential in the microchannels, the streaming potential induced in the nanochannel, and abrupt drop/rise at the interfaces. The streaming potential is an electric potential generated by the directional movement of the non-electroneutral electrolyte through a channel under a pressure gradient (Masliyah and Bhattacharjee 2006). The steep potential change at the interface equivalent to the Donnan potential (Probstein 2003) in the non-flow case leads to strong local electric fields that can be used for analyte preconcentration. The observed potential characteristics can be interpreted by the electrical field behavior in Fig. 3b. The entire nano-microchannel-system can be divided into five sub-domains: two microchannel (electroneutral) segments, a nanochannel (non-electroneutral), and two micro–nano interfaces (enrichment and depletion) featured by the electric field

spikes. In the microchannels, owing to electroneutrality (i.e., $c_{K^+} = c_{Cl^-}$) and the constraint of $I_{tot} = 0$ in Eqs. 5 and 6, the electric field is zero. In the nanochannel, the gradients of the BGE ion concentration are negligible in the longitudinal direction (see Fig. 2a), leading to negligible current contribution from ion diffusion. Therefore, a constant electric field arising from the streaming potential is induced to counteract the convection (flow-carried) current (Masliyah and Bhattacharjee 2006). At the micro–nano interfaces, the scenario is more complicated and the currents from ion diffusion, convection, and migration all are comparable. At the enrichment interface, the diffusive current flux points to the right (i.e., positive, see Fig. 2a). Therefore, the flow and electric field therein need to align to the left and to induce negative current flux to ensure $I_{tot} = 0$ in Eq. 6. In contrast, at the depletion interface ion diffusion aligns with convection (both pointing to the left) to oppose the electromigration-induced current (3rd term in Eq. 6). Hence, the electric field is positive (directing to the right), and gets stronger as the flow rate increases.

To further clarify the dependence of the field strength on the pressure head/flow rate, we perform a simple analysis of the current components in Eq. 6, which is

$$\Gamma_{tot} = -D\nabla\rho_e + \mathbf{u}\rho_e + F\omega(c_{K^+} + c_{Cl^-})(-\nabla\phi) \quad (13)$$

where $\rho_e = F(c_{K^+} - c_{Cl^-})$ is used. In our 2D nanochannel, $dS = dy\hat{i}$ and the total current $I_{tot}$ in Eq. 6 can be expressed as,

$$\begin{aligned} I_{tot} &= \int_S \Gamma_{tot} \cdot dS \\ &= -D\frac{\partial}{\partial x}\int_w \rho_e dy + \int_w \mathbf{u}_x \rho_e dy \\ &\quad + \int_w F\omega(c_{K^+} + c_{Cl^-})(-\nabla\phi)_x dy = 0 \end{aligned} \quad (14)$$

where $\hat{i}$ is the unit vector normal to the channel's cross-section, and subscript $x$ denotes the $x$-components. Equation 14 explicitly depicts the impacts of pressure head (or flow rate) on the ion transport. It shows that the current carried by the bulk flow, i.e., 2nd term in Eq. 14, always aligns to the flow direction, which is pointing to the left in our case. The diffusion current, i.e., 1st term in Eq. 14,

depends on the gradient of the volumetric charge density. In our case, it points to the right at the enrichment interface and to the left at the depletion interface.

Within the nanochannel, due to the local electrical charge conservation, i.e., $\int_w \rho_e dy = \sigma$, Eq. 14 can be recast as

$$\begin{aligned} I_{tot} &= 0 \\ &= -D\frac{\partial\sigma}{\partial x} + \int_w \mathbf{u}_x \rho_e dy + \int_w F\omega(c_{K^+} + c_{Cl^-})(-\nabla\phi)_x dy \end{aligned} \quad (15)$$

where we recall that $\sigma$ is the charge density on the nanochannel surface. In the nanochannel, the 1st term in Eq. 15 is negligible, and the electromigration-induced current (3rd term) counteracts the current resulting from the flow convection (2nd term). Therefore, a higher pressure head gives rise to a larger streaming potential and electric field pointing to the right.

In the vicinity of the enrichment interface, the diffusion current is nearly independent of the pressure head given the constant charges on the nanochannel (see Fig. 2). It is counter-balanced by the combined currents from flow and electromigration. Therefore, as the pressure head increases, the magnitude of the electrical field at the enrichment interface drops off to maintain zero overall current ($I_{tot} = 0$).

At the depletion interface, ion diffusion and convection act against the electromigration current, and hence, a stronger electric field (pointing to the right) is observed at larger pressure heads. For the same reason, the value of the peak electric field at the depletion interface is higher than that at the enrichment interface (see insets in Fig. 3b).

Table 3 summarizes the characteristics of the individual current contributions (viz., $I_{tot,D}$, $I_{tot, conv}$, and $I_{tot, Elec}$) and electric field at the microchannel, nanochannel, and interfaces. At the enrichment interface, it can be anticipated that with a sufficiently large pressure head, convection alone is adequate to offset the molecular diffusion-carried current. Thus, the direction of the electrical field can be reversed to the right (i.e., $E > 0$), which favors the passage of the analytes through the nanochannel and should be obviated in our preconcentration case.

Table 3 Individual current contributions at the microchannel, nanochannel, and interfaces

| | Diffusion current ($I_{tot, D}$) | Convection current ($I_{tot, conv}$) | Electromigration current ($I_{tot, Elec}$) | Electric field ($E = -\nabla\phi$) |
|---|---|---|---|---|
| Microchannel | $I_{tot, D} \approx 0$ | $I_{tot, conv} \approx 0$ | $I_{tot, Elec} \approx 0$ | $E = 0$ |
| Nanochannel | $I_{tot, D} \approx 0$ | $I_{tot, conv} < 0$ | $I_{tot, Elec} > 0$ | $E > 0$ |
| Enrichment interface | $I_{tot,D} > 0$ | $I_{tot, conv} < 0$ | $I_{tot, Elec} = -I_{tot, D} - I_{tot, conv}$ | $\|I_{tot, D}\| \geq \|I_{tot, conv}\|$, $E \leq 0$ |
| | | | | $\|I_{tot, D}\| < \|I_{tot, conv}\|$, $E > 0$ |
| Depletion interface | $I_{tot, D} < 0$ | $I_{tot, conv} < 0$ | $I_{tot, Elec} = -I_{tot, D} - I_{tot, conv} > 0$ | $E > 0$ |
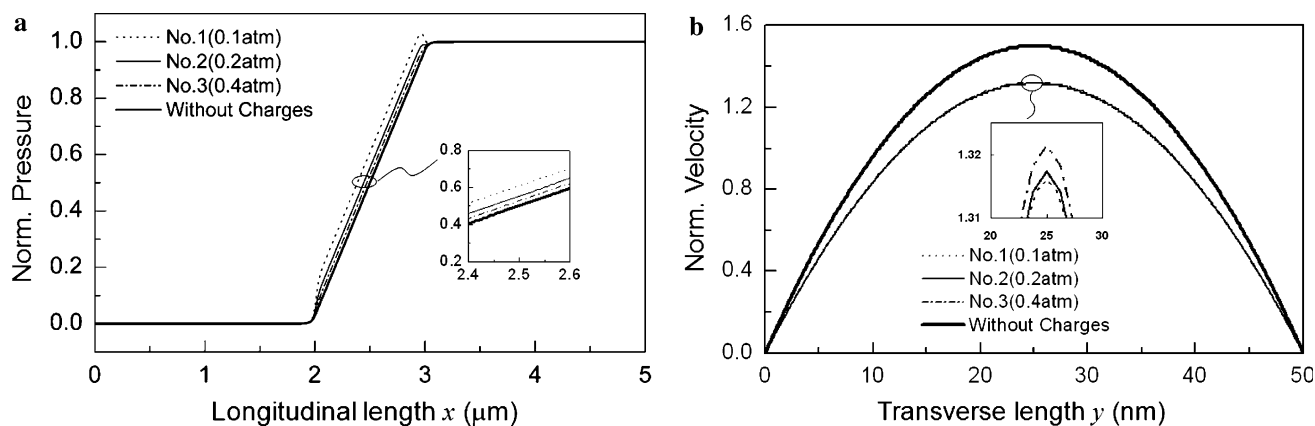
**Fig. 4** Fluidic characteristics (**a**) Longitudinal distribution of normalized pressure. (**b**) Transverse profile of normalized flow velocity

The effects of the induced electrical field on pressure distribution and flow velocity (via the electrostatic body force) are presented in Fig. 4a, b. Figure 4a depicts the longitudinal dependence of the normalized pressure (by the applied pressure head $\Delta p$). Pressure gradient and electrostatic force, in combination drive the fluid flow through the system. It shows that the bulk of the pressure drop takes place in the nanochannel. As the BGE solution is unipolar (positive) in the nanochannel and the electrical field spike around the enrichment interface is directed to the left (i.e., negative), the electrostatic force aligns with the hydrodynamic flow at the enrichment interface (see the $x$-component of the electrostatic force, $f_{e,x} = \rho_e E_x$ in Fig. 5). Thus, smaller (or even reversed) pressure drop at the enrichment interface is needed to conserve the imposed flow rate through the preconcentrator. The pressure in the nanochannel is accordingly raised. The impact of the electrostatic force at the interface is more pronounced when the pressure head is small and the bulk flow is weak. For example, in Case 1 ($\Delta p = 0.1$ atm) the flow rate through the system is extremely low. The electrostatic force at the enrichment interface exceeds the value necessary to maintain such small flow rate and should be balanced by a reverse pressure gradient. Therefore, we observe the pressure-spike at the enrichment interface. On the other hand, the electrostatic force at the depletion interface acts against the flow and needs to be overcome by a large pressure drop (see Fig. 5).

Figure 4b displays the transverse distribution of the normalized flow velocity ($\mathbf{u}/U$) across the nanochannel, where $U$ is the average velocity in the nanochannel in the absence of surface charges at various pressure heads. Since the electrostatic force in the nanochannel counteracts the pressure drop, the flow velocity in all cases is markedly suppressed with respect to the no surface charge case. For the same reason, the effect is the most significant for low-pressure case (see the inset in Fig. 4b).
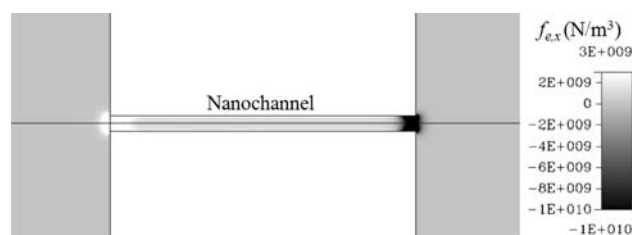


**Fig. 5** Contour of the $x$-component of the electrostatic body force $f_e$

### 3.2.2 Effects of BGE ion concentration

Next we investigate the effect of bulk BGE concentration (Case 2, 4, and 5) on the ion transport and electrokinetics in the micro-nanofluidic preconcentrator. Figure 6a illustrates longitudinal profile of BGE ion concentrations, and the observations are similar to those in the previous section. As the bulk BGE concentration in the microchannel increase, the ion profiles are elevated as a whole. Figure 6b reveals the transverse ion concentration profile across the nanochannel. At low BGE ion strength (Cases 2 and 4), the EDL at both channel walls are heavily overlapped; hence the solution is essentially unipolar with counter-ions ($K^+$) and the ion profiles are identical regardless of the bulk concentration. However, in a more concentrated solution (e.g., 1 mM in Case 5) the overlap between the EDLs is alleviated and the amount of $K^+$ and $Cl^-$ ions are comparable. Thus, a micro-nanochannel interconnect becomes "leaky" and the ion concentrations in the system are closer to bulk concentrations.

Figure 7 depicts the longitudinal distribution of the electrical potential and electric field at various BGE ion concentrations. It shows that as the BGE concentration decreases, the streaming potential, potential drop/rise at the interface, and the overall potential all increase, leading to stronger electrical field in the nanochannel and interfaces. Detailed insight into this observation can be gained by investigating Eqs. 14 and 15.
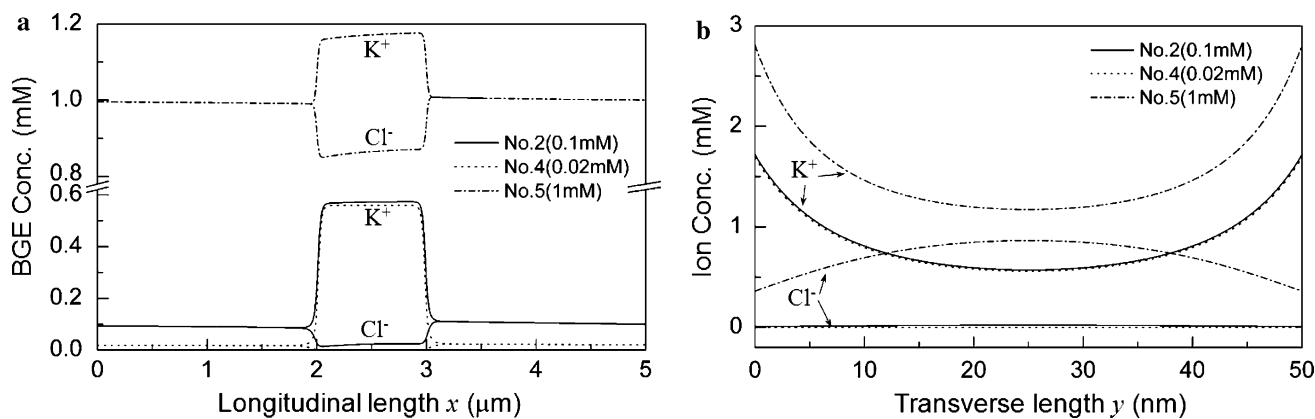
**Fig. 6** Profiles of BGE ion concentrations. (**a**) Longitudinal profile (**b**) Transverse profile
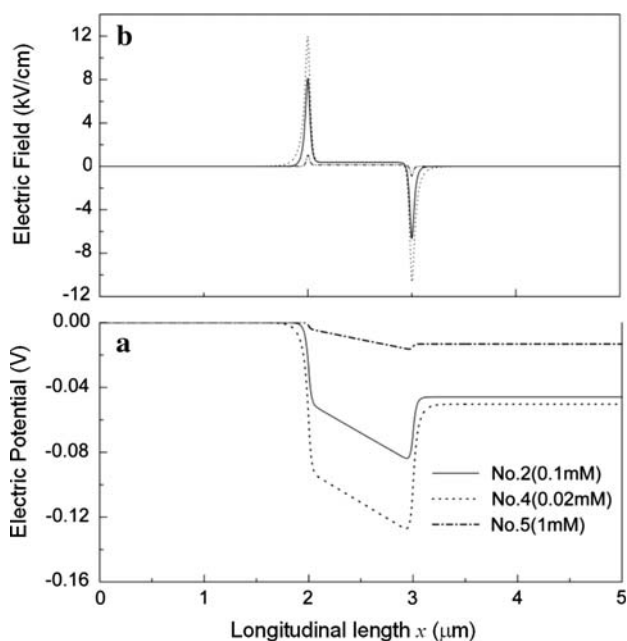


**Fig. 7** Longitudinal profiles of (**a**) electrical potential and (**b**) field

In the nanochannel, the diffusion current (the 1st term in Eqs. 14 and 15) is negligible. At a higher BGE concentration, the EDL is thinner and volumetric charges mostly distribute at the region close to the channel wall (see Fig. 6b) where flow velocity is very low, leading to smaller convection current. As a result, the electromigration current and the electric field both decrease to ensure $I_{tot} = 0$, which is also manifested by the lower streaming potential in Fig. 7a. A point of note is that there is virtually no increase in the electrical field from Case 4 (0.02 mM) to Case 2 (0.1 mM). This is attributed to the unipolar nature of the BGE solution in the nanochannel, viz., the ion distribution therein is independent of the bulk concentration supplied from the microchannel.

At the interface, the diffusion current and convection current are less susceptible to the bulk BGE ion concentration than the electromigration current as the latter is explicitly proportional to the total ion concentration ($c_{K^+} + c_{Cl^-}$). Hence, the constraint of $I_{tot} = 0$ is mostly preserved via the constancy in electromigration current. Thus, for a more concentrated bulk solution in the microchannel, the electric field at the interface has to decrease as illustrated in Fig. 7b.

Figure 8a reveals the longitudinal dependence of the normalized pressure and Fig. 8b illustrates the transverse profile of the normalized flow velocity. Similar to the previous observations on the effect of pressure head, small/reversed pressure drop and abrupt pressure drop are, respectively, identified at the enrichment and depletion interface for dilute BGE solution, because of the stronger electric field and electrostatic force. Flow in all cases appreciably slows down due to the electrostatic force acting against the pressure drop in the nanochannel. The deviation from the no surface charge case is most distinct at lower bulk BGE concentrations that generate stronger electric fields in the nanochannel. Table 4 summarizes the effects of the overall pressure head and bulk BGE concentration on the electrokinetic behavior at various regions.

### 3.3 Simulation of analyte enrichment

In this section, we present the transient simulation results to investigate the effects of the operating parameters (pressure head and BGE concentrations) and analyte properties on analyte enrichment. Three sample analytes (A–C) are used, with diffusivity $\{D_A, D_B, D_C\} = \{2 \times 10^{-11}, 2 \times 10^{-11}, 1 \times 10^{-11}\}$ m$^2$/s and effective mobility $\{z_A\omega_A, z_B\omega_B, z_C\omega_C\} = \{-1 \times 10^{-8}, -0.5 \times 10^{-8}, -1 \times 10^{-8}\}$ m$^2$/(Vs). Analyte A, which is treated as the benchmark sample, differs from analyte B and analyte C, respectively, in terms of mobility and diffusivity. Analyte concentrations
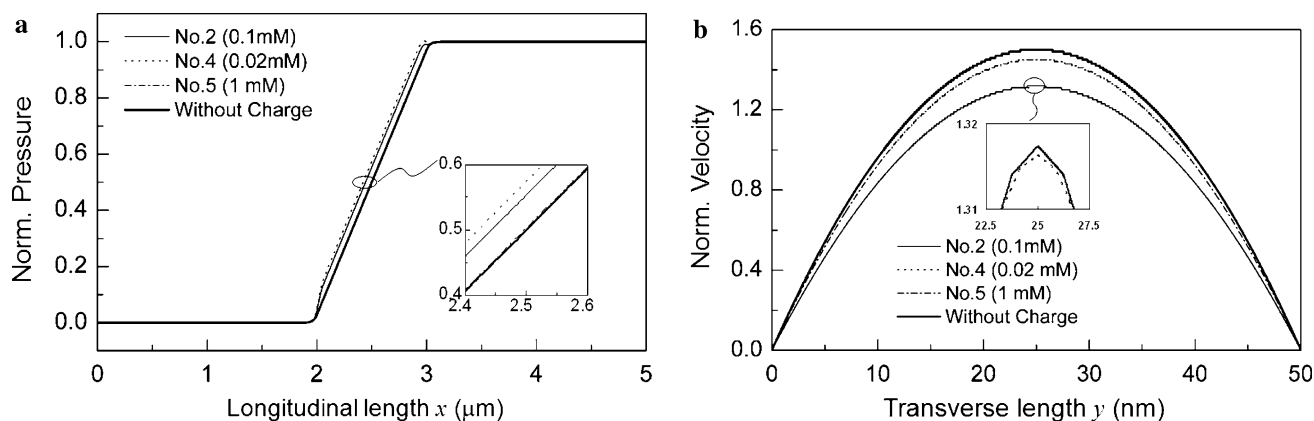
**Fig. 8** Fluidic characteristics (**a**) Longitudinal distribution of normalized pressure. (**b**) Transverse profile of normalized flow velocity

**Table 4** Effect of pressure head and BGE concentration on the electrokinetic behavior at various regions

|  | Ion concentration | Electric field | Flow velocity |
|---|---|---|---|
| Decrease in pressure head |  |  |  |
| Microchannel | $c_{bulk}$ | 0 | Decrease |
| Nanochannel | Decrease | Decrease | Decrease |
| Enrichment interface | Decrease | Increase | Decrease |
| Depletion interface | Increase | Decrease | Decrease |
| Decrease in bulk BGE ion concentration |  |  |  |
| Microchannel | $c_{bulk}$ | 0 | Decrease |
| Nanochannel | Decrease | Increase | Decrease |
| Enrichment interface | Decrease | Increase | Decrease |
| Depletion interface | Decrease | Increase | Decrease |

($c_{anal,in} = 1$ nM) of analytes A–C are specified uniformly at the inlet. To characterize the preconcentrator performance, an index of enrichment ratio (ER), viz. the ratio of the maximum analyte concentration in the computational domain to that at the inlet, is defined. The position of the maximum analyte concentration depends on the electric field at the interface and analyte properties, and is different from case to case.

Figure 9a depicts the concentration contour of analytes A–C in the baseline case (Case 2) at the end of simulation ($t = 2$ s). Note that different scales are used for clarity. We can see that the analytes are concentrated at the region in front of the enrichment interface and the preconcentration heavily depends on the analyte properties. Figure 9b illustrates the effects of the analyte properties on ER. It is straightforward that analyte B has a lower electrophoretic mobility, and hence, experiences weaker electromigration force at the interface, resulting in lower ER. On the other hand, the lower diffusivity of analyte C reduces the diffusion flux into the channel and yields a higher ER, approaching $10^4\times$.

Figure 10 illustrates the transient evolution of ER of Analyte A in all operating cases (Table 2). While all ERs increase with the time for all cases, they eventually approach different steady state values. Relative to the baseline case (Case 2), Case 3 and Case 5 that employ a larger pressure head and more concentrated BGE solution, respectively, lead to lower ER and faster arrival of the steady state. On the other hand, extremely high ER is
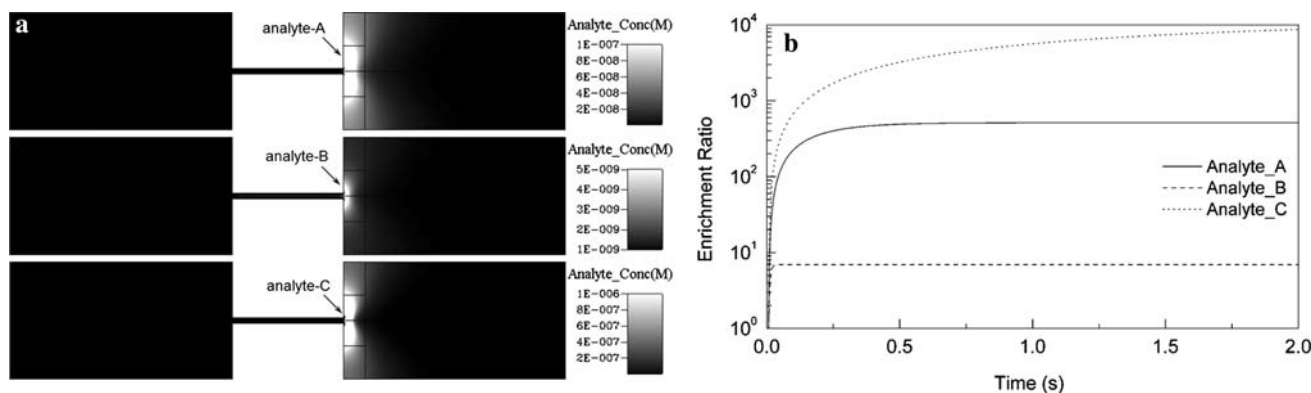


**Fig. 9** Preconcentration of all analytes (A–C). (**a**) Concentration contour. (**b**) Transient evolution of ER in operating Case 2 (baseline case)
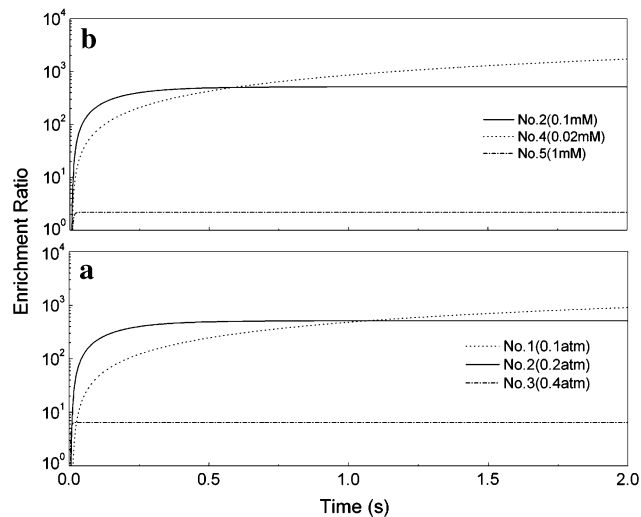
**Fig. 10** Transient evolution of ER of Analyte A in all operating cases. (**a**) Effects of pressure head. (**b**) Effects of BGE ion concentrations

observed in Cases 1 and 4, which involve a lower pressure head and lower BGE concentration, respectively. This is due to the fact that at the micro–nano interface, the electromigration force imposed on the negatively charged analytes points to the right and prevents the analyte from entering the nanochannel, while the diffusion flux and hydrodynamic force act in the opposite direction. Therefore, large pressure head (large **u** in Case 3) and concentrated BGE solution (lower electric field $-\nabla\phi$ in Case 5) favor the ingress of the analytes into the channel and produce lower ER. The relationship between the enrichment ratio and the BGE concentrations qualitatively agrees with the experimental observation in (Plecis et al. 2005b).

## 4 Conclusion

A framework for numerical analysis was presented to investigate the BGE ion transport and analyte transport in a micro-nanofluidic interconnect preconcentrator. The simulation relies on the direct, coupled solution of the governing equations and was conducted in a two-step manner assuming dilute analyte concentrations. The numerical results were validated against analytical models of simplified, canonical cases, and excellent agreement was obtained. Parametric analysis was undertaken to develop insights into the impact of critical operating parameters, pressure head and BGE concentration, on the electrokinetic ion transport in the system. Appreciable concentration–polarization is observed between the two micro–nano interfaces due to the inhibitive passage of co-ions through the nanochannel and imbalanced ion flux at the interface.

The Donnan potential at the interface induces substantial electric field barrier (>1 kV/cm in our cases) and the large field strength occurs at low pressure head and low BGE concentration. Relative to the case without surface charge, presence of the charges on the nanochannel surface suppresses the bulk flow (electro-viscous effect).

Studies were also conducted to describe the effects of the analyte properties and operating parameters on analyte enrichment. In addition to the hydrodynamic force, the repulsive electrophoretic force has to overcome substantial diffusional flux of the analyte. Therefore, analytes with smaller diffusivity and higher electrophoretic mobility experience stronger enrichment. Further, within the practically relevant range, the BGE concentration and pressure head should be maintained low to augment the electric field barrier and slow down the hydrodynamic flow for salient preconcentration. Our simulation also demonstrates that with properly configured parameters, order-of-magnitude enrichment can be achieved. The analysis presented in this paper provides critical insights into the electrokinetics in the hydrodynamic flow-based micro-nanofluidic preconcentrator and can be utilized to guide device design and protocol development for next generation microsystems.

## References

Bharadwaj R, Santiago JG (2005) Dynamics of field-amplified sample stacking. J Fluid Mech 543:57–92

Daiguji H, Yang PD et al (2004a) Ion transport in nanofluidic channels. Nano Lett 4(1):137–142

Daiguji H, Yang PD et al (2004b) Electrochemomechanical energy conversion in nanofluidic channels. Nano Lett 4(12):2315–2321

Daiguji H, Oka Y et al (2005) Nanofluidic diode and bipolar transistor. Nano Lett 5(11):2274–2280

Daiguji H, Oka Y et al (2006) Theoretical study on the efficiency of nanofluidic batteries. Electrochem Commun 8(11):1796–1800

Ehlert S, Hlushkou D et al (2008) Electrohydrodynamics around single ion-permselective glass beads fixed in a microfluidic device. Microfluid Nanofluid 4(6):471–487

Feng JJ, Krishnamoorthy S et al (2006) Simulation of electrokinetic flow and analyte transport in nano channels. 2006 NSTI Nanotechnology Conference and Trade Show, Boston, pp 505–508

Huang KD, Yang RJ (2008) Formation of ionic depletion/enrichment zones in a hybrid micro-/nano-channel. Microfluid Nanofluid 5(5):631–638

Jin XZ, Joseph S et al (2007) Induced electrokinetic transport in micro-nanofluidic interconnect devices. Langmuir 23(26):13209–13222

Kim SM, Burns MA et al (2006) Electrokinetic protein preconcentration using a simple glass/poly(dimethylsiloxane) microfluidic chip. Anal Chem 78(14):4779–4785

Kim SJ, Wang YC et al (2007) Concentration polarization and nonlinear electrokinetic flow near a nanofluidic channel. Phys Rev Lett 99(4):044501

Leinweber FC, Pfafferodt M et al (2005) Electrokinetic effects on the transport of charged analytes in biporous media with discrete ion-permselective regions. Anal Chem 77(18):5839–5850

Lichtenberg J, de Rooij NF et al (2002) Sample pretreatment on microfabricated devices. Talanta 56(2):233–266

Mansouri A, Scheuerman C et al (2005) Transient streaming potential in a finite length microchannel. J Colloid Interf Sci 292(2):567–580

Masliyah JH, Bhattacharjee S (2006) Electrokinetic and colloid transport phenomena. Wiley-Interscience, Hoboken, NJ

Patankar SV (1980) Numerical heat transfer and fluid flow. Taylor & Francis, Washington, New York

Plecis A, Schoch RB et al (2005a) Ionic transport phenomena in nanofluidics: Experimental and theoretical study of the exclusion-enrichment effect on a chip. Nano Lett 5(6):1147–1155

Plecis A, Schoch RB et al (2005b) On-chip separation and concentration processes based on the use of charge selective nanochannels. Micro Total Analysis Systems, Transducers Research Foundation, Boston, MA, USA, pp 1038–1041

Probstein RF (2003) Physicochemical hydrodynamics. An introduction. John Wiley & Sons, New York

Pu QS, Yun JS et al (2004) Ion-enrichment and ion-depletion effect of nanochannel structures. Nano Lett 4(6):1099–1103

Shackman JG, Ross D (2007) Counter-flow gradient electrofocusing. Electrophoresis 28(4):556–571

Sueyoshi K, Kitagawa F et al (2008) Recent progress of online sample preconcentration techniques in microchip electrophoresis. J Separation Sci 31(14):2650–2666

Wang YC, Han JY (2008) Pre-binding dynamic range and sensitivity enhancement for immuno-sensors using nanofluidic preconcentrator. Lab Chip 8(3):392–394

Wang YC, Stevens AL et al (2005) Million-fold preconcentration of proteins and peptides by nanofluidic filter. Anal Chem 77(14):4293–4299

Xuan XC, Li DQ (2004) Analysis of electrokinetic flow in microfluidic networks. J Micromech Microeng 14(2):290–298